Supplementary Information

Omnidirectional and effective salt-rejecting absorber with rational-designed nanoarchitecture for efficient and durable solar vapour generation

Xiaoying Song[†‡], Hucheng Song[†], Ning Xu[†], Huafeng Yang[†], Lin Zhou[†], Linwei Yu[†], Jia Zhu[†], Jun Xu*[†‡], Kunji Chen[†]*

[†]*School of Electronics Science and Engineering, National Laboratory of Solid State Microstructures/Collaborative Innovation Center of Advanced Microstructures and College of Engineering and Applied Sciences, Nanjing University, Nanjing 210093, China*
[‡]*Jiangsu Provincial Key Laboratory of Advanced Photonic and Electronic Materials, Nanjing University, Nanjing 210093, China*
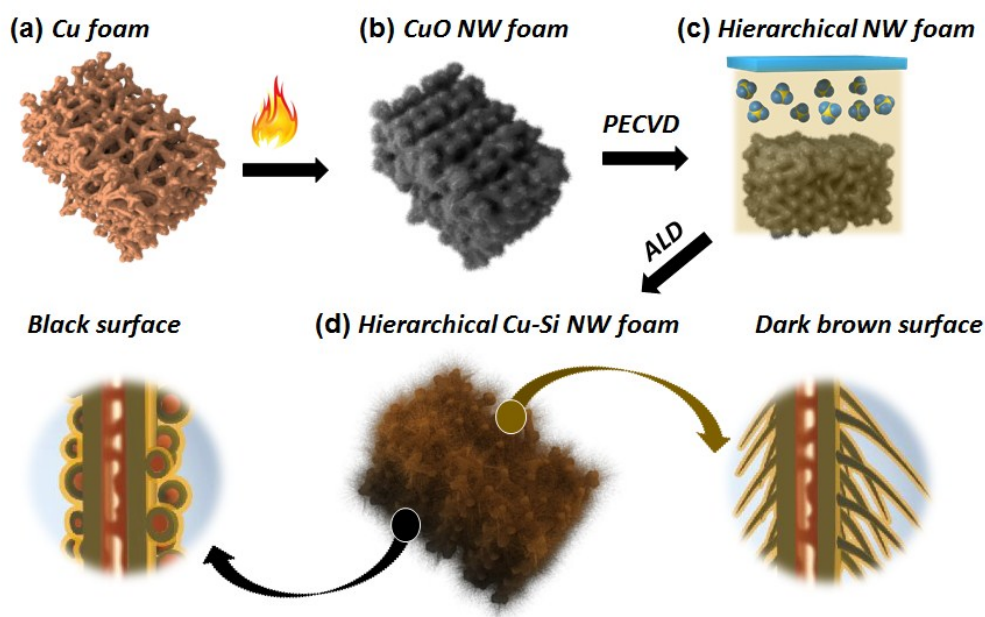
Fig. S1 Preparation process of hierarchical copper silicon nanowire (HCS NW) porous membrane. A schematic illustration of the preparation of HCS NW structure grown on copper foam (CF). (a) Copper foam. (b) Copper oxide (CuO) nanowire foam after thermal oxidation growth in atmosphere. (c) Coating amorphous silicon (a-Si), tin (Sn) thin film and grafting Si NWs on CuO NWs, respectively, and finally obtained hierarchical CuO/c-Si

(HCOS) NW structures grown overall foam substrate in a PECVD system. (d) Hierarchical copper-silicon (HCS) NW porous membrane with a light-receiving surface (RLS, black) and root-like water pumping surface (LRS, dark brown) after a high temperature H_2 annealing and ALD process.

A hierarchical bottom-up strategy was used to prepare the HCS NW porous membrane that includes four basic processes as shown in Fig. S1. First, the copper oxide (CuO) NWs were prepared on the porous foam substrate by typical thermal oxidation process. Then, the sample was loaded into a plasma enhanced chemical vapor deposition (PECVD) system and an amorphous silicon film was deposited on freely growing CuO NWs by a glow discharge deposition of SiH_4. In the next step, a tin (Sn) film (~5 nm) was prepared CuO/a-Si core shell NWs by a thermal evaporation system. During this preparation process of catalyst, tin (Sn) is very difficult to deposit on the back of CuO/a-Si core shell NW foam that contact with stainless steel sample stage in the thermal evaporation equipment, thus failing to induce the growth of Si NW branches on the side during Sn catalyzed VLS growth process. After that, crystal silicon nanowires (c-Si NWs) were grafted upon amorphous silicon (a-Si) coated copper oxide (CuO) core shell NWs by a typical Sn catalyzed vapor-liquid-solid (VLS) process and then a high-temperature H_2 annealing process (600 °C) was employed to reduce copper-oxide/silicon complex structures. During a high-temperature H_2 annealing process, the CuO NW cores were reduced to Cu, which could then diffuse into and even out the thin silicon shell to form self-sustainable Cu NPs/Cu-Si NW hybrid structure (Fig. 1f). Hence, the formation of Cu NPs assembled Cu-Si NW structure is caused by the reduction of CuO and diffusion of Cu in silicon at a high-temperature H_2 annealing process. After coating an Al_2O_3 thin layer using atomic layer deposition (ALD), a single-layer structured Cu-Si porous membrane was obtained that consists of two typical NW-hierarchical structures: Al_2O_3 coated Cu NPs/Cu-Si nanowire light-receiving structures (black, LRS) and Al_2O_3 coated c-Si/Cu-Si nanowire root-

like structures (dark brown, RLS) grown on both sides of the porous copper foam, respectively.
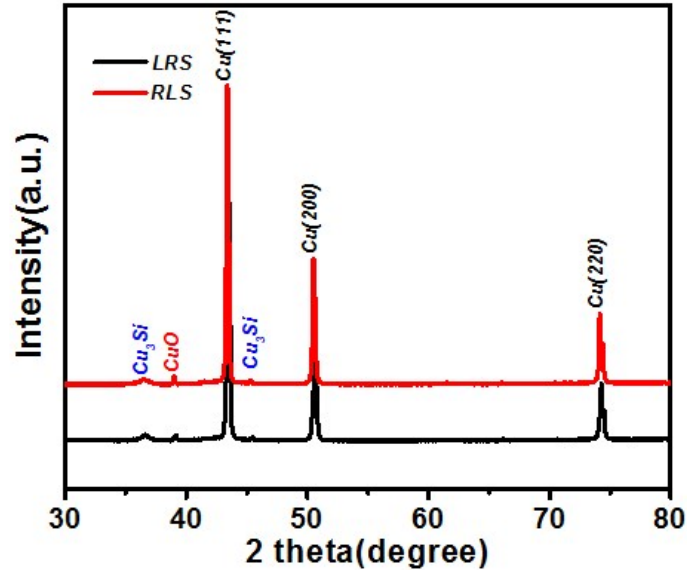

Fig. S2 XRD analysis of the LRS and RLS of the HCS NW membrane.

According to the X-ray diffraction (XRD) analysis shown in Fig. S2, a high-temperature H_2 annealing at 480°C has been sufficient to activate the alloy-forming process of copper silicon, leading to the strongest diffraction peaks located at 43.4°, 50.5° and 74.3°, respectively, which correspond to the crystalline planes of Cu (111), (200) and (220). Meanwhile, two addition peaks emerge at ~36.5° and 45° corresponding to the two strongest diffraction peaks of Cu_3Si. This indicates that the CuO cores can be effectively reduced to Cu that then continues to diffuse and alloy with silicon (including both the a-Si outer shell layer and the c-Si NWs branch) during the high-temperature H_2 annealing process. In addition, we also observed a weak diffraction peak located at ~48° that indicated an emergency of CuO phase.
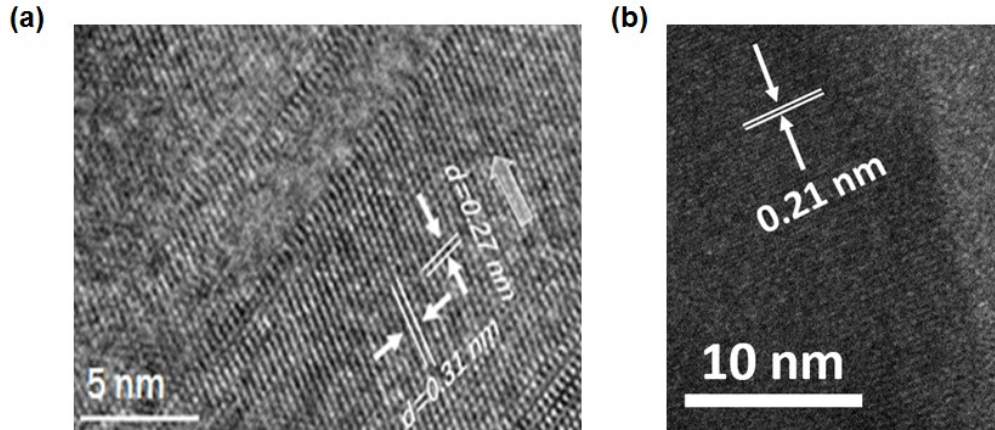
Fig. S3. High-resolution TEM images of the HCS NW structure. (a) Crystal silicon (c-Si) NW branch. (b) Copper silicon (Cu-Si) trunk.

To assess the detailed structural information, high-resolution transmission electron microscopy (HRTEM) was used to characterize the c-Si NW branch and Cu-Si alloy trunk of the HCS NW structure. The growth orientation of the cubic Si NW branch along [211], corresponding to d=0.27 nm, has been confirmed as seen in Fig. S3a. Meanwhile, the HRTEM result clearly show a discontinuous and hollow Cu core in Cu-Si alloy trunk. This can be further confirmed by the X-ray diffraction (XRD) spectra in Fig. S2, in which the emergence of three new and the strongest diffraction peaks located at 43.4°, 50.5° and 74.3°, respectively, which belong to the crystalline planes of Cu (111), (200) and (220).
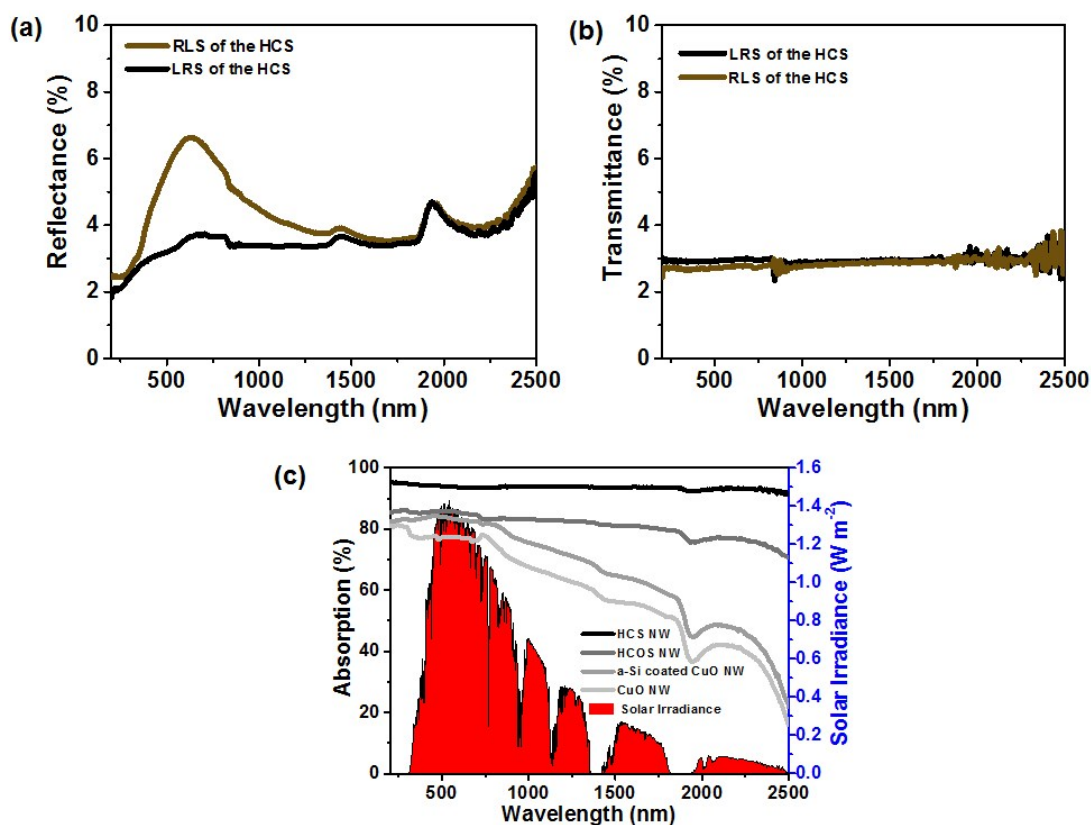
Fig. S4. Transmission, reflection and absorption spectrum of the HCS NW membrane.

(a, b) The reflection and transmission spectrum of LRS (black, Al_2O_3 coated CuNP/Cu-SiNW) and RLS (dark brown, Al_2O_3 coated c-SiNW/Cu-SiNW) of the HCS NW porous membrane. (c) Absorption spectrum of the HCS NW, HCOS NW, a-Si coated CuO NW and CuO NW porous membrane.

Fig. S4 shows the light absorption property of the HCS NW porous membrane. The reflectance (Fig. S4a) and transmission spectrum and (Fig. S4b) show an efficient and broadband solar adsorption of the HCS NW porous membrane from UV, visible to near infrared light. Both the LRS (Al_2O_3 coated NP/NW) and the RLS (Al_2O_3 coated NW/NW) of the membrane demonstrate the very low transmittance (<3% for LRS and <7% for RLS) and reflectance (<3% for both surface) at 200-2500 nm. As shown in Fig. S4c, the HCS NW porous demonstrates an efficient broadband absorption of solar spectrum irradiation with a more than ~93.8% at 200-2500 nm. This light absorption capability is

greatly superior to hierarchical CuO/c-Si NW (HCOS NW, 85% at visible light irradiation range), a-Si coated CuO NW core-shell (a-Si/CuO NW, ~82% at visible irradiation range) and CuO NW (~78% at visible light irradiation range) porous membrane as well as other Si-based materials.
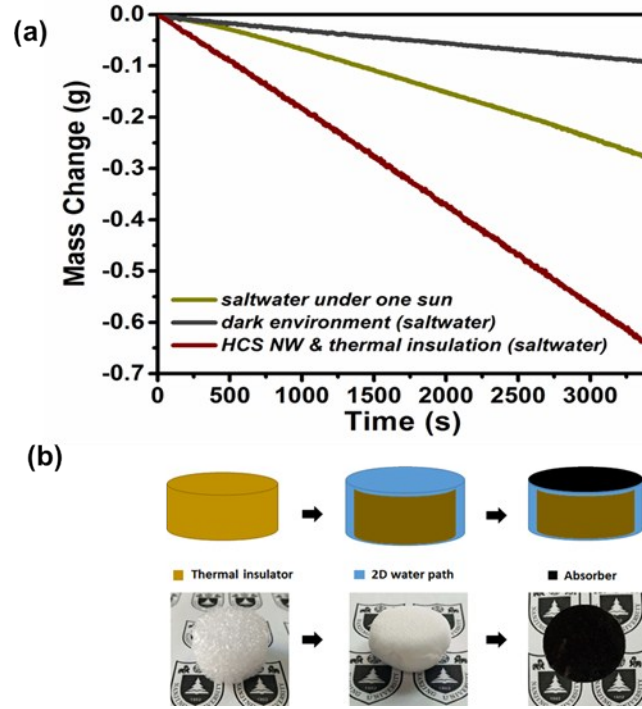

Fig. S5. (a) Saltwater evaporation performances of the HCS NW with thermal insulation layer, dark environmental of the double-layer structure and pure saltwater under one-sun irradiation, respectively. (b) Flowchart for the fabrication of solar desalination devices: polystyrene foam, cellulose coating, and HCS NW membrane. The physical map of polystyrene foam (thermal insulator, Left), cellulose wrapped over the surface of polystyrene foam (2D water path, Middle) and HCS NW membrane (absorber, Right).

Fig. S5a shows the saltwater evaporation performances of the HCS NW with thermal insulation layer. The mass flux m is calculated by the following formula:

$$m = m_{HCS} - m_{dark} - \frac{S_1 - S_2}{S_1} m_{water} \qquad (1)$$

where m_{hcs} is the evaporation rate of the HCS NW & thermal insulation structure

under 1 sun irradiation, which is 1.92×10^{-4} g/s. m_{dark} is the dark environment evaporation rate of the HCS NW & thermal insulation structure without sun irradiation, which is 0.26×10^{-4} g/s. m_{water} is the water evaporation rate without HCS NW & thermal insulation structure under 1 sun irradiation, which is 0.97×10^{-4} g/s. S_1 is mouth area of Dewar container(4.52 cm^2), S_2 is the sample area(4.15 cm^2). The evaporation rate is calculated from the slope of the curve at stable state (the last 60 seconds) in Figure S5a.

Fig. S6. (a, b) High-resolution XPS spectra of the RLS and the LRS after saline cycles (7 pure-water and 15 saline cycles) for a long time (10 months). (c) EDX bulk elemental and corresponding XRD structures (d) of the RLS and LRS of the HCS NW membrane after saline cycles (7 pure-water and 15 saline cycles) for a long time (10 months).

To explore the surface composites of the membrane, we conducted high-resolution X-ray photoelectron spectroscopy (XPS) analysis on both the RLS

(Fig. S5a) and LRS (Fig. S5b) after a long cycle. The surface of the RLS (Al2O3 coated c-SiNW/Cu-Si NW in Fig.6b) soaked in saline is largely composed of carbonates, hydrocarbons and sodium chloride[44-46]. For the surface of LRS, Na_{1s} (at ~1070.6 eV, corresponding carbonate) is observed for the LRS of the HCS NW membrane, in which no chlorine signal is found (Fig. 6g). Moreover, a hydrophobic carbon-oxygen functional group (corresponding to C1s peak at 285.7 eV) is detected at the surface of the LRS (Fig. 6h) that result in a decreasement of the water contact angle of RLS as shown in Fig. 6c. As shown in Fig. 4c, the contact angle of LRS decreases from the 122° (the first saline cycle) to 113° (the 15th saline cycle) after a long-term saline cycle that indicate the formation of stable interface hybrid layer including a sodium compound and a carboxyl group. Fig. S5c shows the EDX elemental analysis and XRD structure analysis of the LRS and the RLS of the HCS NW porous membrane after a 22 cycles (7 pure water cycles and followed 15 saline cycles). As shown in Fig. S5c, the EDX bulk elemental analysis show a trace NaCl (<4%) emerging on both the RLS and RLS of the HCS NW porous membrane after a long time saline cycle, which indicate a high salt-rejection of the HCSNW porous membrane. Fig. S5d shows the XRD structure analysis of the LRS and RLS of the porous membrane where the strongest diffraction peaks located at 43.4°, 50.5° and 74.3°correspond to the crystalline planes of Cu (111), (200) and (220), respectively. The addition peaks emerge at ~32.5°, 42.5° and 45° corresponding to the diffraction peaks of Cu_3Si and the other peaks are from CuO phases. The crystal structure of both the LRS and RLS has not any change and no other diffraction peaks are found comparted to the XRD result of the initial HCS membrane (See in supplementary Fig. S2). These results indicate a robust and stable structure of the HCS NW porous membrane even after a long time saline cycle.
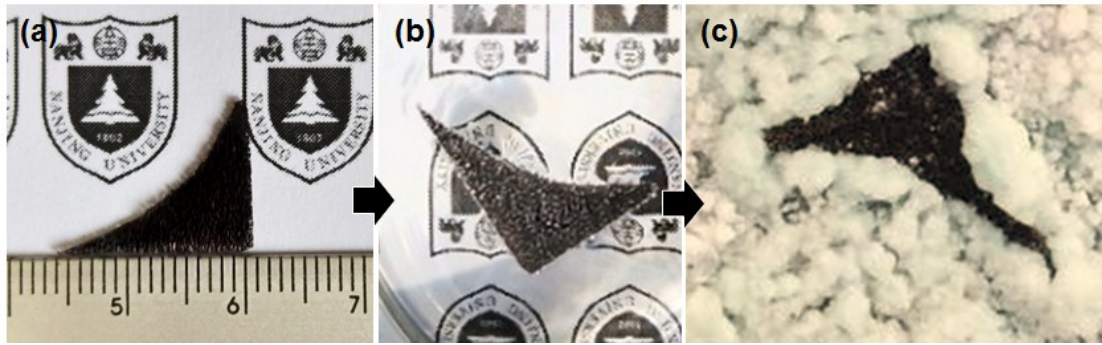
.

Fig. S7. Photograph of the HCS NW porous membrane. (a) Photograph of the HCS NW porous membrane. (b) Photograph of the HCS NW porous membrane floating on the surface of saline (with 20.0% NaCl). (c) Photograph of the hierarchical HCS NW porous membrane after several weeks saline evaporation.

Fig. S6 shows the photograph of the HCS NW porous membrane. To study the anti-salt capability of the HCS NW porous membrane, we employed a HCS NW porous membrane with gradient size distribution (~0.5 mm to 3.2 cm as shown in Fig. S6a). As shown in Fig. S6b, this membrane can well float on the surface of the saline. After a long-time nature light irradiation (about several weeks), the water was completely evaporated and the salt is deposited as shown in Fig. S6c. Surprisingly, the black LRS (Al_2O_3 coated CuNP/Cu-Si NW) remain a fresh and clean surface even at the very sharp places (Fig. S6c). We also observed that the NaCl crystals only attach to the sidewalls of the membrane and fail to form a salt coating on the surface of the membrane even at small-scale sharp corners with a width of ~0.5 mm. That result a failure occupy of salt for the light-receiving surface of our membrane. This capability is superior to most solar absorbers [21] where dense and crowded salt crystals are formed on the whole membrane during a long-term solar irradiation, which indicates the HCS NW membrane could act as an effective NaCl-rejecting membrane and long-time use for solar desalination.
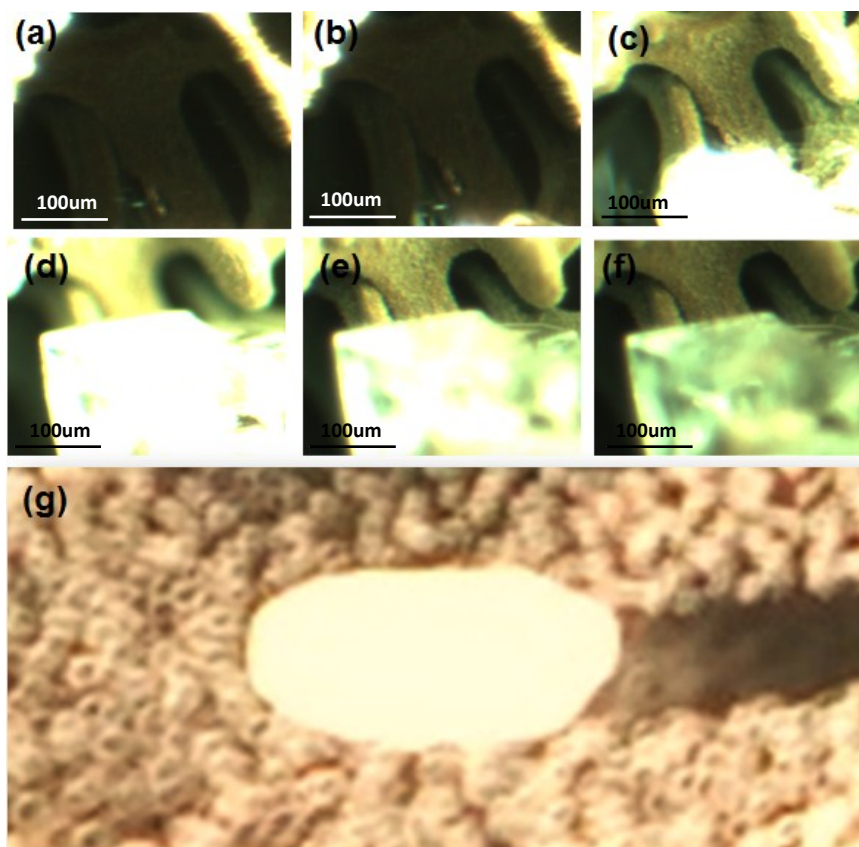
Fig. S8. In-situ real-time observation of a drop saline (with 20%. wt) on the surface of the HCS NW porous under Xe-lamp irradiation. (a) 0 min, (b) 15min, (c) 17 min, (d) 19 min, (e) 20 min and (f) 21 min. (g) the photograph of the saline drop after the water is completely evaporated.

Fig. S8 shows the in-situ optical microscope of a saline drop on the surface of the HCS NW porous membrane after the water is completely evaporated under Xe-lamp irradiation. Fig. S8a show the initial photograph of saline drop on the surface of the HCS NW porous membrane. After 17 min solar irradiation, the saline drop size is shrinking and the clear edge of the NaCl crystal is presented in Fig. S8c. With the further shrinking of the saline drop, NaCl crystal continuously grow and finally form a completely crystal on the surface of the membrane (Fig. S8f and S8g). This salt-crystal is supported by the HCS NW structure instead of penetrating into the interior of the membrane vis micro-pores (~ 50 um-200 um), which clearly suggests an effective salt rejection of

the HCS NW structure even at a higher saline concentration (~20 wt.% NaCl) for a long-term solar light irradiation.
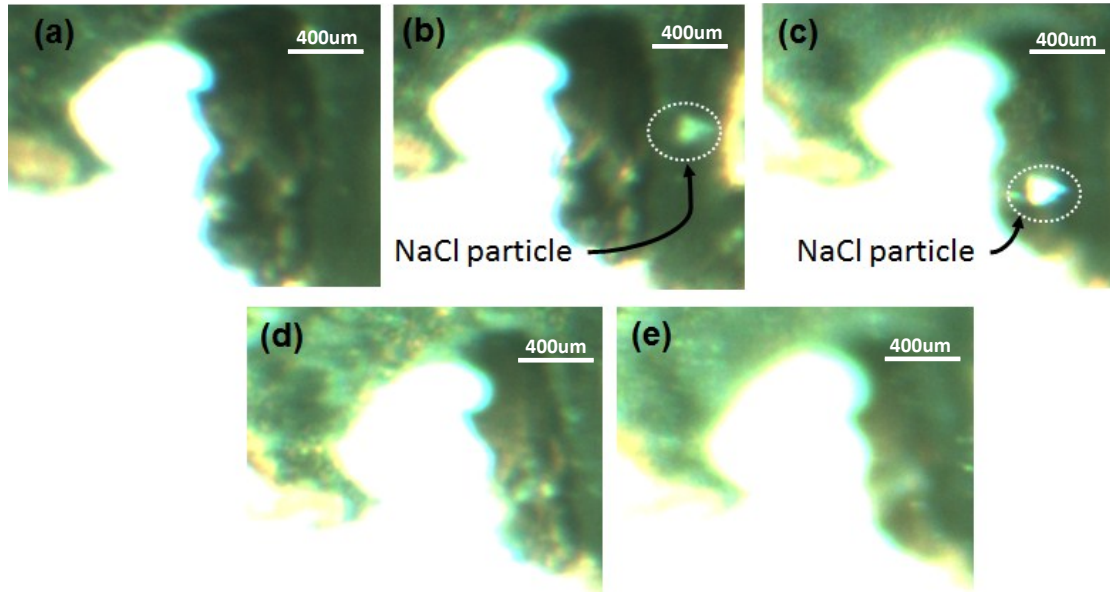

Fig. S9. In-situ real-time observation of the surface of the HCS NW porous floating on the saline (20%. wt) surface under Xe-lamp irradiation. (a) 0 h, (b) 1260 min, (c) 1270 min, (d) 1280 min, (e) 1290 min.

In situ real-time microscope observation was also used to study the solar desalination process of the membrane under high-power density Xe-lamp irradiation in high concentration saline (20%.wt). We can observe that the membrane could withstand long-time durability where the edge of the front surface is free of salt accumulation in saline water even at a high concentration saline of 20%. The morphology of the edge morphology of the membrane has not changed after a long time saline test (1290 min, see in Fig. S8e) than that of the initial morphology (0min, see in Fig. S8a), which indicates a robust structure of the HCS NW membrane during a long time durability test (even in 20% saline). In addition, we also observed that the pre-formed NaCl particle on the surface of the membrane is dissolved in the subsequent evaporation process due to the robust super-hydrophobic feature of our designed structures.

S10 (Table 1). A summary of the performances of state-of-the-art solar vapour generation devices published recently in top journals [7, 9, 11, 13, 17, 20, 48-52] in comparison to what is achieved in this work.

Materials & Structure	Absorption （%）	Omni-directional Light to Heat	Efficiency (%)	Cyclical Stability	Salt-rejecting Capability	Desalination result	Insulation layer	Ref.
Carbonized Mushrooms	≈96%	---	≈78	---	---	---	Yes	48
Plasmonic Wood	≈99	--- (absorption)	≈68	144 h	Yes	---	---	49
Porous Graphene	≈90	---	≈80	---	---	---	---	7
Graphdiyne-Based CuO NWs	≈92	---	≈91	20 h	---	---	---	20
Graphene oxide-based membrane	≈94	---	≈80	10 h	---	<5mg l^{-1}	Yes	24
Black gold membranes	≈91	---	≈35	---	---	---	---	9
Al NP/AAM	≈96	---	≈58	25 h	---	<1mg l^{-1}	---	11
Black TiOx Nanoparticles	≈91.3	---	≈50	---	---	---	---	17
Nanostructured gels	≈95	---	≈94	50 h	---	<5mg l^{-1}	---	13
Hydrophilic black cellulose fabric	≈85	---	≈57	---	Yes	---	Yes	50
Environmental energy-enhanced generator	---	---	>100%	---	---	<1mg l^{-1}	---	51
Environmental energy-enhanced generator	---	---	>100%	---	---	---	---	52
Hierarchical Cu-Si NW membrane	**≈93.8**	**Yes**	**≈86**	**310 day**	**Yes**	**<1mg l^{-1}**	**Yes**	**Our**

S11. Steady-State Energy Balance Analysis

The input heat flux (J_{in}) is 1 kw/m^2. The five main strategies for energy consumption exists: (1) water evaporation, (2) reflection energy loss, (3) conductive heat loss from sample to water, (4) radiation heat loss from sample to the environment, (5) convection heat loss from sample to the environment. For the highest evaporation efficiency (86%) of the HCS NW porous membrane with a thermal insulation layer, in our work, the total energy consumption is

assessed by the following equations.

1) *Water evaporation consumption* η_C:

The water evaporation consumption is the water evaporation efficiency that is **~86%**.

2) *Refection and transmission losses* $\eta_{ref,\ C}$:

The solar absorption of our membrane is 93.8%. Therefore, the total loss $\eta_{ref,c}$ of the transmission and refection is **~6.2%** that is calculated the equation (A+R+T=100%).

3) *Conduction loss* $\eta_{cond,\ N}$:

The device was put in a Dewar container under one-sun irradiation to calculate the conduction loss. The Conductive heat flux from sample to water J_{cond} is calculated based on equation (1):

$$J_{cond} = Cm\Delta T \qquad (1)$$

C is the specific heat capacity of water (4.2 J g^{-1}°C^{-1}), m is the mass of the water in the Dewar container, ΔT is the temperature difference of the water before and after t , and t is the irradiation time. In our experiment, t = 3600 s, m = 25 g, ΔT = 0.5 °C, and *A* is the surface area of the Dewar container, which is about 4.52 cm^2. Thus, J_{cond} is about 52 J.

The conduction loss $\eta_{cond,\ N}$ is calculated based equation (2):

$$\eta_{cond,\ N} = \frac{J_{cond}}{J_{in}} \frac{1}{t * A} = 3.2\% \qquad (2)$$

The conductive loss $\eta_{cond,\ N}$ is around 3.2% that is mainly caused by the thermal insulation layer with relatively low thermal conductivity where the calculation method of the conduction loss referred to the ref. [1]. Notably, the calculation of the conduction loss includes the contribution of the water which was exposed to the one-sun irradiation. Therefore, the calculation result of the conduction

loss (3.2%) is exaggerated for this part.

4) Radiation loss $\eta_{rad, N}$:

The radiation loss is calculated by Stefan- Boltzmann, as shown in equation (3).

$$J_{rad} = \varepsilon\sigma(T_1^4 - T_2^4) \qquad (3)$$

J_{rad} is the heat flux, σ is the Stefan−Boltzmann constant (5.67*10⁻⁸ Wm⁻²K⁻⁴). ε is the emissivity (0.92) that is calculated by Planck's law and the absorbance of our membrane. T_1 is the average temperature of the absorber (31.2 °C in our system). T_2 is the room temperature (25℃). Therefore, we can calculate the J_{rad} is 35.3 Wm⁻² according to Equation (3).

The radiation heat loss of the device is calculated by the equation (4):

$$\eta_{rad, N} = \frac{J_{rad}}{J_{in}} = \frac{35.3 w/m^2}{1000 w/m^2} = 3.5\% \qquad (4)$$

The calculated result indicates a radiation loss $\eta_{rad, N}$ of around 3.5% where the calculation way of the radiation loss was reported in supplementary ref. [1].

(5) Convection loss $\eta_{conv, N}$:

The convection heat flux was calculated by Newton' law of cooling.

$$P_{conv} = hA\Delta T \qquad （5）$$

$$\eta_{conv, N} = \frac{P_{conv}}{J_{in}} \qquad （6）$$

Among them, h is convection heat transfer coefficient, A is surface area of the sample (4.15cm²). ΔT is the difference between the absorber surface temperature (31.2 ℃ in our system) and the ambient temperature(25℃ in our system). According to early report in supplementary ref [2], the convection heat transfer coefficient is about 5 Wm⁻²K⁻¹. ΔT is about 6.2 ℃ in our experimental.

Therefore, the convective heat loss is about 3.1%. This calculation way was also reported in supplementary ref. [3].

Therefore, the total value of these five main energies is about 99.2% (86% + 6.2% + 3.2% + 3.5%+3.1% ≈ 102%). Except the exaggerated conduction loss in part 3), the total energy is close to 100%. The other solar energy may be dissipated by the test system or other ways.

Reference

[1] X.Q. Li, W.C. Xu, M.Y. Tang, L. Zhou, B. Zhu, S.N. Zhu, J. Zhu, *Proc Natl Acad Sci USA* 2016, 6, 13953-13958.

[2] H. Ghasemi, G. Ni, A. M. Marconnet, J. Loomis, S. Yerci, N. Miljkovic, G. Chen, *Nat. Commun.* 2014, 5, 4449.

[3] N. Xu, X.Z. Hu, W.C. Xu, X.Q. Li, L. Zhou, S.N. Zhu, J. Zhu, *Adv. Mater.* 2017, 29, 1606762.